Inorganic Chemistry

pubs.acs.org/IC

Article

Negative Linear Compressibility and Interlayer Gap Closure in Layered Rare-Earth Hydroxyhalide ($YCl(OH)_2$) under High Pressure

Mengzeng Wu, Jingui Xu,* Dongzhou Zhang, Yi Zhou, Wei Chen, Shanrong Zhang, Qifa Zhong, and Dawei Fan*

Cite This: *Inorg. Chem.* 2024, 63, 2616−2626

Read Online

ACCESS | Metrics & More | Article Recommendations | Supporting Information

ABSTRACT: Layered materials have attracted extensive attention due to their exceptional physical and chemical properties. Understanding the structural evolution of such materials under high pressure is crucial for the development of new functional materials. In this study, the structure evolution of the synthesized layered rare-earth hydroxyhalide $YCl(OH)_2$ under high pressures up to approximately 9.4 GPa was explored by using a diamond anvil cell combined with synchrotron single-crystal X-ray diffraction. Simultaneously, high-pressure Raman spectroscopy experiment was conducted to 10.3 GPa. Our findings indicate that $YCl(OH)_2$ maintains its symmetry within the experimental pressure range. The pressure−volume data of $YCl(OH)_2$ were fitted to the third-order Birch−Murnaghan equation of state (EoS) to derive its EoS parameters including zero-pressure unit-cell volume (V_{T0}), isothermal bulk modulus (K_{T0}), and its pressure derivative (K'_{T0}): V_{T0} = 142.47 (1) Å^3, K_{T0} = 38.2 (18) GPa, and K'_{T0} = 9.8 (1). However, the unit-cell parameters *a*, *b*, and *c* exhibit a distinct compressional behavior, with the *a*-axis being the most compressible and the *b*-axis being the least. Particularly noteworthy is the observation that $YCl(OH)_2$ displays a negative linear compressibility along the *b*-axis within the pressure range of 0.4−5.3 GPa. Further detailed structure refinement and Raman spectroscopy analyses indicate that the anomalous behavior of the *b*-axis could be attributed to the formation of the O−H···O hydrogen bonding chains along the *b* direction. Moreover, the coordination number of Y^{3+} increased from 8 to 9 as the pressure reached 5.3 GPa due to the reduction of the interlayer spacing upon compression, ultimately leading to the closure of the interlayer gap.

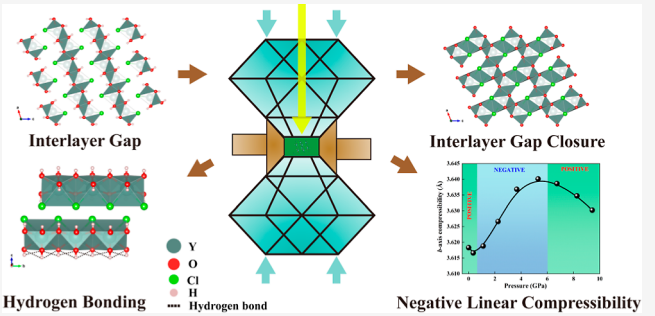

Downloaded via ARGONNE NATL LABORATORY on May 28, 2024 at 20:21:50 (UTC).
See https://pubs.acs.org/sharingguidelines for options on how to legitimately share published articles.

1. INTRODUCTION

Rare-earth elements (REEs) are of significant industrial importance and are often referred to as the "modern industrial vitamins" and the "treasure trove of 21st century materials." Due to their exceptional thermal, mechanical, optical, electrical, and magnetic properties, REEs are frequently utilized as additives in other compounds or metal alloys.[1,2] This utilization leads to the creation of a wide range of unique materials with distinct performance characteristics. Therefore, REEs are extensively utilized in strategic emerging industries, including defense and military technology, aerospace, electronics and information technology, and new energy sources, among others. Moreover, their growing significance has elevated them to be pivotal and strategic mineral resources for global economic development and societal progress.[3,4]

On the other hand, layered hydroxides are extensively used in various fields, such as catalysis, pharmaceuticals, photochemistry, and electrochemistry, owing to their distinctive crystal structure. Layered rare-earth hydroxides (LREHs) combine the exceptional physical and chemical properties of REEs with the characteristic crystal structures of layered hydroxides. This combination makes LREHs promising contenders for diverse industrial applications in the aforementioned fields.[5] Consequently, since the 1960s, researchers from multiple domains have engaged in extensive studies on LREHs, exploring their synthetic methods, crystal structures, and various other physical and chemical properties.[6−9] However, halide ions can substitute certain hydroxyl groups within layered hydroxides, leading to the formation of layered hydroxyhalides.[10] Whether layered rare-earth hydroxyhalides have the same or even more unique properties than LREHs is unknown.

High pressure serves as a powerful tool for manipulating material properties, allowing for the modification of the crystal structure of materials to enhance their industrial applica-

Received: November 6, 2023
Revised: January 7, 2024
Accepted: January 11, 2024
Published: January 24, 2024

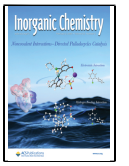

ACS Publications

© 2024 American Chemical Society

tions.[11,12] Exploring the evolution of crystal structure and elasticity properties of LREHs under high-pressure conditions not only facilitates a deeper comprehension of the physical and chemical properties of these materials but also plays a crucial role in the development of new functional materials.[13] However, to the best of our knowledge, no research has been reported thus far regarding the evolution of crystal structure and elastic properties under high-pressure conditions, even for structurally simple LREHs, let alone layered rare-earth hydroxyhalides.[14]

Therefore, in this study, we successfully synthesized single-crystal samples of layered rare-earth hydroxyhalide ($YCl(OH)_2$) under high-temperature and high-pressure conditions (200 °C and 0.02 GPa). By employing a diamond anvil cell (DAC) apparatus in conjunction with synchrotron single-crystal X-ray diffraction (SCXRD), we conducted the inaugural exploration of its compressibility, crystal structure evolution, elastic properties, and the pressure-induced modulation of interlayer spacing at high pressures.

2. SAMPLE AND EXPERIMENTS

2.1. Synthesis of the $YCl(OH)_2$ Crystal. The synthesis of $YCl(OH)_2$ crystals was conducted through a room-temperature mixing and high-temperature maturation growth experimental technique, employing the conventional stainless steel autoclave with an inner Teflon bottle at 0.02 GPa and 200 °C. The reagents used in the experiment were hexahydrated yttrium chloride ($YCl_3 \cdot 6H_2O$, 99.9%, metals basis) produced by Shanghai Aladdin Biochemical Technology Co., Ltd., and sodium bicarbonate ($NaHCO_3$, 99.99%, metals basis) produced by Shanghai Macklin Biochemical Co., Ltd. The experiment employed a conventional hydrothermal reaction vessel with a Teflon liner and an outer stainless steel high-pressure vessel. The Teflon liner consists of two parts, with a total volume of 10 mL, including a bottle and a matching bottle cap. The height of the stainless steel autoclave is 70 mm, and the outer diameter is 45 mm, while the height of the Teflon bottle is 55 mm, with outer diameters of 32 mm and inner diameters of 20 mm. The filling degree of the whole equipment is 43%. At first, 2.7 mL of 0.5 mol/L YCl_3 solution and 1.6 mL of 1 mol/L $NaHCO_3$ solution were added directly into the Teflon bottle and mixed. The Teflon bottle with the mixture was then transferred to an external stainless steel autoclave, ensuring a secure seal to prevent leakage during the experiment. Finally, the autoclave with the inner Teflon bottle and the mixture was placed in a tube furnace and subjected to a programmed reaction at 200 °C and about 0.02 GPa for 1 month, with both heating and cooling gradients set at 100 °C per hour. Following the completion of the reaction, the solution and products in the Teflon bottle were poured into the centrifugal tube and were centrifuged to extract the precipitate. Then, the precipitate was washed three times alternately with deionized water and anhydrous ethanol. Finally, the white precipitate was dried at 60 °C, and $YCl(OH)_2$ crystals were acquired from the precipitate. The crystals were colorless and transparent and exhibited a needlelike shape with lengths less than 500 μm (Figure 1).

$YCl(OH)_2$ crystals, with an approximate size of 300 μm, were selected for electron microprobe analysis (EMPA). The analysis was performed using a JXA8230 tungsten filament electron probe microscope at the Institute of Geochemistry, Chinese Academy of Sciences, operating at an acceleration voltage of 25 kV, with a beam current of 20 nA and a beam diameter of 1 μm. The chemical formula was determined as $Y_{1.00}Cl_{1.00\pm0.03}[(OH)_{1.00\pm0.03}]_2$ based on the EMPA data.

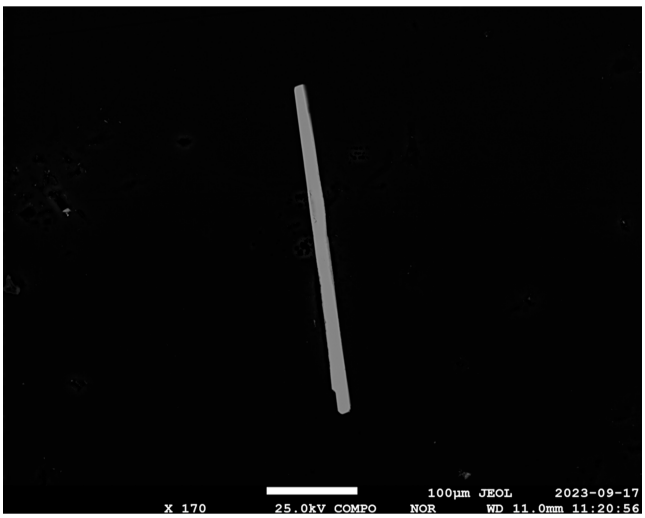

Figure 1. Backscattered image of synthetic $YCl(OH)_2$ crystals.

2.2. High-Pressure Single-Crystal X-ray Diffraction. We utilized a BX90-type DAC, equipped with a pair of symmetric diamond anvils, whose culet diameters were 500 μm. A 250 μm-thick rhenium gasket was initially indented at the central area to a thickness of approximately 70 μm. Subsequently, a 300 μm diameter hole was created as the sample chamber in the center of the indentation by using a laser puncher. $YCl(OH)_2$ single-crystal samples and a ruby pressure standard were placed within the sample chamber, followed by gas-loading with helium as the pressure-transmitting medium, and the pressure inside the chamber was determined by measuring the ruby's fluorescence spectrum.[15] The pressure was measured both before and after collecting the sample data, and the average was used.

In situ high-pressure synchrotron SCXRD experiments were conducted at the 13-BM-C beamline, Advanced Photon Source, Argonne National Laboratory. SCXRD experiments were performed under both ambient and high-pressure conditions using a six-circle diffractometer. The incident X-ray wavelength was 0.4340 Å, and the beam size was 12 μm × 18 μm. SCXRD images were acquired by utilizing a PILATUS 1 M detector. The detector tilts, rotations, and sample-to-detector distance were calibrated using LaB_6 powder.[16] The Φ rotation step size was 0.5°, and the measurement exposure time was 1°/s. For a detailed description of the experimental procedure, please refer to Zhang *et al.* (2017).[16] Diffraction data were collected at two different detector positions (D1 and D2) achieved by rotating the detector on the six-circle goniometer. At D1, the detector was perpendicular to the incident X-ray direction, while D2 was achieved by rotating the detector about the horizontal axis by 20°.

In this experiment, diffraction data were collected at nine different pressures ranging from ambient pressure to 9.4 (1) GPa. Initially, the diffraction data were analyzed using *APEX*3 software to obtain unit-cell parameters and volume and derive structure factors for crystal structure determination and refinement. The detector failed to rotate to the D2 position during our data collection at 5.3 GPa, so only the peaks collected at the D1 position were used for the structural refinement. We found that the data at the 8.3 GPa pressure point were insufficient to obtain reliable structural refinement

https://doi.org/10.1021/acs.inorgchem.3c03909
Inorg. Chem. 2024, 63, 2616−2626

results; therefore, this point was not selected in the structural refinement. Subsequently, crystal structure solution and refinement were carried out using the *SHELX* program[17] facilitated by the *Olex*2 graphical interface.[18] Hydrogen atoms were not considered in the structure refinement process at high pressure, as the number of acquired diffraction peaks was limited by the DAC. For the same reason, anisotropic thermal parameter models were only applied to *Y* atoms during structure refinement. Bond lengths and polyhedral parameters were calculated using *VESTA* software.[19]

2.3. Raman Spectroscopy. The high-pressure and ambient-temperature Raman spectroscopy experiments were performed at the Center for High Pressure Science and Technology Advanced Research (HPSTAR), China. The Raman spectra of the sample were acquired by a Renishaw InVia spectrometer equipped with a Peltier-cooled charge-coupled device detector. During the experiments, the samples were excited by a laser at 532 nm, and the laser spot was focused to a diameter of about 1 μm using a Leica 50× telephoto lens with a laser power of 2 mW. A single-crystal silicon wafer was used to calibrate the wavenumber of the Raman shift before the measurement.

$YCl(OH)_2$ single-crystal sample and a ruby sphere, which was used as the pressure calibrator, were loaded into the sample chamber. Raman spectra data were collected at 12 pressure points from ambient pressure to 10.31 GPa. The Raman spectra of the sample were collected with an exposure time of 20 s. According to the previous Raman study[20] on $REE(OH)_3$ which is analogous to our $YCl(OH)_2$, the collected Raman spectra ranges were 100−1200 and 3000−4000 cm^{-1}. The peak positions (Raman shift) were obtained by Gaussian peak fitting. In addition, no uncommon hazards are noted in all of our experiments.

3. RESULTS

The symmetry of $YCl(OH)_2$ remained in $P2_1/m$ up to the maximum pressure attained in this study. The unit-cell parameters and volumes of $YCl(OH)_2$ at different pressures are presented in Table 1 and Figures 2 and 3. Analysis of the XRD data collected under ambient pressure condition generated the following unit-cell parameters and volume: a = 6.216 (1) Å, b = 3.6183 (1) Å, c = 6.6234 (2) Å, β = 106.99 (1)°, and V = 142.474 (8) Å^3. As the pressure increased, as shown in Figure 2, the unit-cell parameters a, c, and the volume V gradually decreased. At the maximum pressure of 9.4 GPa, a = 5.772 (5) Å, c = 6.4353 (13) Å, and V = 124.58 (1) Å^3. In contrast, b decreased with increasing pressure within 0−0.4 GPa, followed by an increase from 0.4 to 5.3 GPa, reaching 3.6401 (3) Å and subsequently decreasing again to 3.6302 (3) Å from 5.3 to 9.4 GPa. Simultaneously, β gradually increased with increasing pressure, and β = 112.49 (3)° at 9.4 GPa.

Table 1. Unit-Cell Parameters and Volume of $YCl(OH)_2$ at Different Pressures[a]

P (GPa)	a (Å)	b (Å)	c (Å)	β (deg)	V (Å^3)
0.0001	6.216 (1)	3.6183 (1)	6.6234 (2)	106.9 9 (1)	142.47 (1)
0.4 (1)	6.189 (6)	3.6166 (3)	6.6007 (13)	107.07 (3)	141.23 (12)
1.1 (1)	6.136 (4)	3.6188 (2)	6.5775 (8)	107.80 (2)	139.06 (8)
2.2 (1)	6.041 (6)	3.6266 (4)	6.5494 (17)	108.90 (4)	135.75 (14)
3.7 (1)	5.975 (4)	3.6368 (2)	6.5321 (1)	110.46 (2)	132.98 (9)
5.3 (1)	5.897 (6)	3.6401 (3)	6.5071 (14)	111.45 (3)	130.01 (12)
6.7 (1)	5.857 (5)	3.6386 (3)	6.4834 (9)	112.06 (2)	128.06 (11)
8.3 (1)	5.802 (6)	3.6347 (3)	6.4557 (12)	112.37 (3)	125.90 (12)
9.4 (1)	5.772 (5)	3.6302 (3)	6.4353 (13)	112.49 (3)	124.58 (1)

[a]Numbers in parentheses represent standard deviations to the last significant digit.

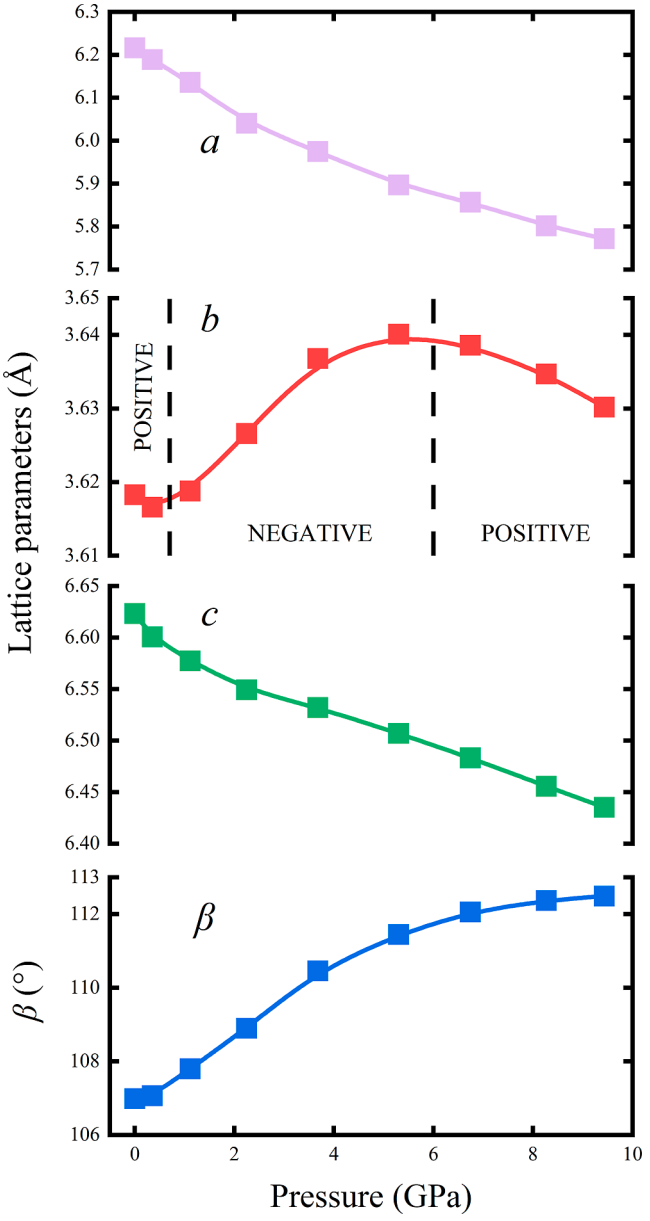

Figure 2. Unit-cell parameters a, b, c, and β up to 9.4 GPa. The dashed lines outline the unusual compressional behavior change of b. Error bars are smaller than the symbols when not shown.

The experimental data above indicate that as pressure increases, the unit-cell volume V decreases without any discontinuities. Therefore, the equation of state (EoS) parameters of $YCl(OH)_2$ were obtained by fitting the pressure−volume data to the third-order Birch−Murnaghan equation (BM3)

https://doi.org/10.1021/acs.inorgchem.3c03909
Inorg. Chem. 2024, 63, 2616−2626

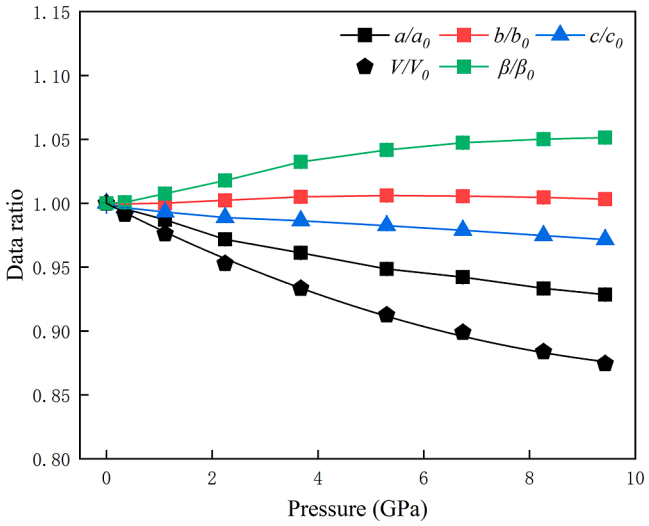

Figure 3. Unit-cell parameters *a*, *b*, *c*, *β*, and volume *V* up to 9.4 GPa. Error bars are smaller than the symbols when not shown. Each curve is normalized to the initial value of each parameter under ambient conditions.

$$P = (3/2)K_{T0}[(V_{T0}/V)^{7/3} - (V_{T0}/V)^{5/3}] \times [1 + (3/4)(K'_{T0} - 4)[(V_{T0}/V)^{2/3} - 1]] \quad (1)$$

where V_{T0}, V, K_{T0}, and K'_{T0} represent the zero-pressure unit-cell volume, high-pressure unit-cell volume, zero-pressure isothermal bulk modulus, and its pressure derivative, respectively. Using the *EosFit7-GUI* software,[21] fitting of the pressure−volume data yielded V_{T0} = 142.47 (1) Å^3, K_{T0} = 38.2 (18) GPa, and K'_{T0} = 9.8 (1).

As shown in Figure 4, we employed the Eulerian strain (f_E = $[(V_0/V)^{2/3} - 1]/2$)−normalized pressure ($F_E = P/[3f_E(2f_E + 1)^{5/2}]$) plot ($F_E - f_E$ plot;[22]) to assess the quality of the EoS fitting. A linear fitting of the $F_E - f_E$ data yielded an intercept value, $F_E(0)$ = 38.2 (9) GPa, and the slope of the fitted line was positive, consistent with the values of K_{T0} = 38.2 (18) GPa and K'_{T0} = 9.8 (1) obtained from the BM3 EoS fitting. Therefore, the use of BM3 EoS to fit the experimental data is reasonable.

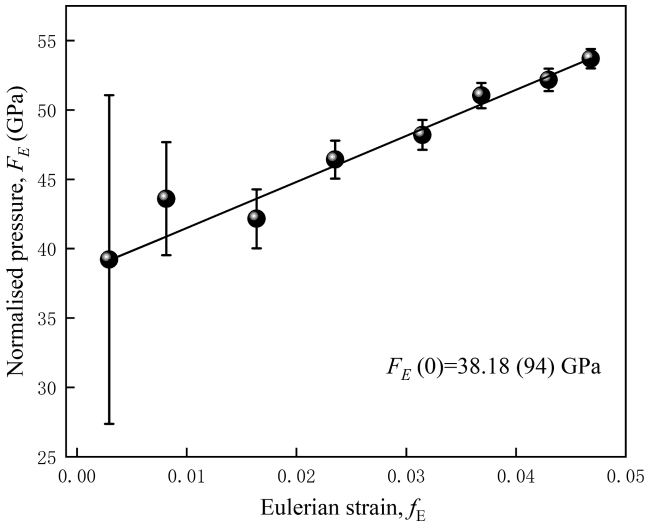

Figure 4. Volumetric Eulerian strain-normalized pressure ($F_E - f_E$) plot.

Using single-crystal XRD data, we performed structural determination and refinement of the examined sample (Table 2). The results reveal that the $YCl(OH)_2$ crystal exhibits a monoclinic crystal system with the $P2_1/m$ space group. As shown in Figure 5, at ambient pressure, each Y^{3+} is coordinated with 6 O^{2-} and 2 Cl^-, forming a YO_6Cl_2 polyhedron. The average cation−anion distance (d) within this polyhedron is 2.4846 Å. Specifically, d_{Y-O1a} = 2.392 (1) Å, d_{Y-O1b} = 2.329 (1) Å, d_{Y-O2a} = 2.337 (1) Å, d_{Y-O2a} = 2.38 (1) Å, and d_{Y-Cl} = 2.853 (17) Å (Figure 5 and Table 3). The volume of this polyhedron is $V(YO_6Cl_2)$ = 25.90 Å^3, with a distortion index of 0.0742.

Table 2. Structural Refinement Details of $YCl(OH)_2$ at Different Pressures[a]

P (GPa)	0.0001	0.4 (1)	1.1 (1)	2.2 (1)
R_{int} (%)	1.97	3.37	2.85	2.97
R_1 (all reflections, %)	0.0198	0.0378	0.0297	0.031
R_1 (Fo > 4sig(Fo))	0.0197	0.0337	0.0285	0.0297
wR_2 (all reflections, %)	0.0495	0.0911	0.1069	0.0866
goodness of fit	1.073	1.236	1.383	1.323
no. of total reflections	3008	288	298	305
no. of reflections (Fo > 4sig(Fo))	771	128	116	117
no. of fitting parameters	32	16	16	16
P (GPa)	3.7 (1)	5.3 (1)	6.7 (1)	9.4 (1)
R_{int} (%)	3.78	3.37	2.64	10.25
R_1 (all reflections, %)	0.0483	0.0337	0.028	0.1047
R_1 (Fo > 4sig(Fo))	0.0378	0.0337	0.0264	0.1025
wR_2 (all reflections, %)	0.1184	0.0773	0.0616	0.2942
goodness of fit	1.303	1.264	1.089	1.248
no. of total reflections	289	233	261	269
no. of reflections (Fo > 4sig(Fo))	111	54	102	113
no. of fitting parameters	16	16	16	16

[a]Numbers in parentheses represent standard deviations to the last significant digit.

As pressure increases, the cation−anion distances within the YO_6Cl_2 polyhedron exhibit irregular variations (Figure 6a,b and Table 3), indicating that the distances between Y and Cl/O atoms within the polyhedron are not significantly influenced by pressure within the pressure range. At 9.4 GPa, d_{Y-O1a} = 2.230 (60) Å, d_{Y-O1b} = 2.370 (80) Å, d_{Y-O2a} = 2.290 (40) Å, d_{Y-O2b} = 2.58 (18) Å, and d_{Y-Cl} = 2.853 (17) Å. As the pressure increases from ambient pressure to 3.7 GPa, the volume of the YO_6Cl_2 polyhedron gradually decreases to 25.07 Å^3, increases to 25.19 Å^3 at 5.3 GPa, and then decreases to 23.77 Å^3 as the pressure increases to 9.4 GPa (Figure 6c and Table 3). The pressure dependence of the distortion index of the YO_6Cl_2 polyhedron is very similar to that of the polyhedral volume, and inflection occurs at 5.3 GPa. In the pressure range from ambient pressure to 3.7 GPa, the distortion index gradually increases to 0.0775. When the pressure increases from 3.7 to 5.3 GPa, the distortion index decreases to 0.0760 and then rapidly increases to 0.0916 with further pressure increase (Figure 6d).

While a total of 18 Raman active modes are anticipated for $YCl(OH)_2$ based on group theory analysis,[23] only 16 modes were observed under ambient conditions (Figures 7a and S1). Notably, a previous study[24] delved into Raman spectroscopy

https://doi.org/10.1021/acs.inorgchem.3c03909
Inorg. Chem. 2024, 63, 2616−2626

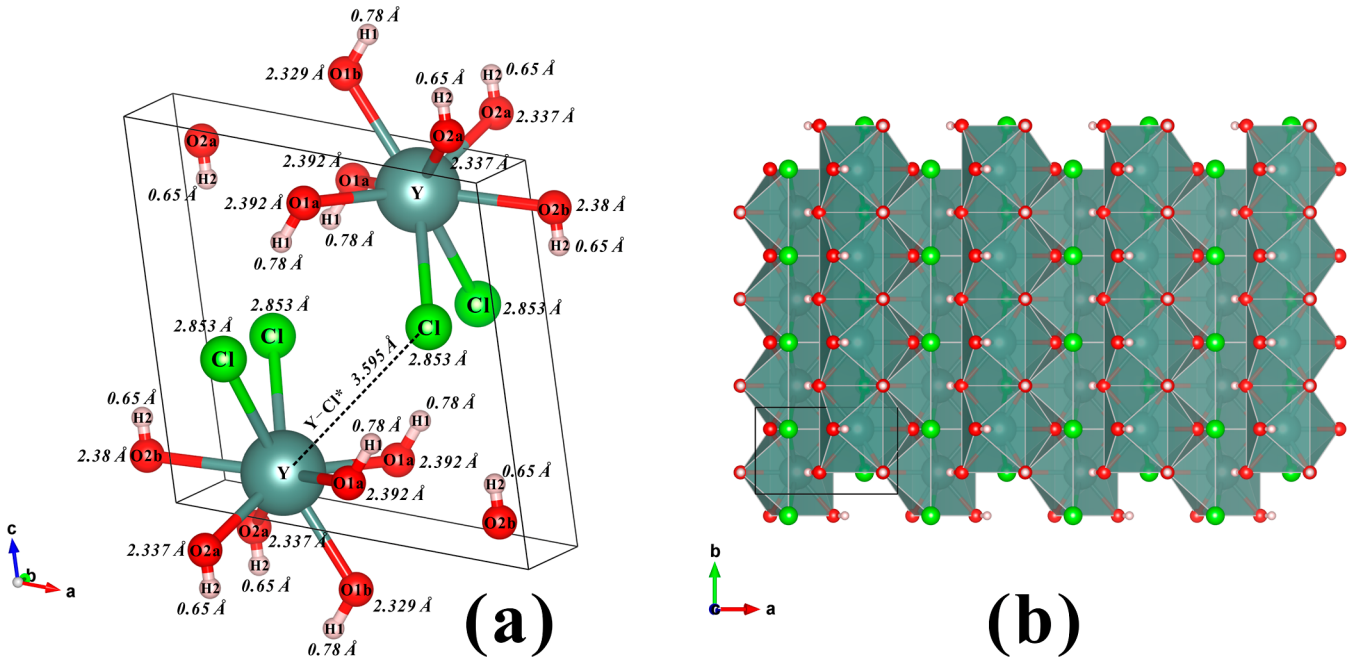

Figure 5. (a) Crystal structure of $YCl(OH)_2$. Y atoms are represented in dark green, Cl atoms in green, O atoms in red, and H atoms in pink. Dashed lines indicate the distance (Y–Cl*) between the Y atom and its nearest Cl atom in the adjacent coordination polyhedron. The atomic distance for each one is shown nearby. (b) $YCl(OH)_2$ coordination polyhedra unfolding along the a–b plane.

for several $REECl(OH)_2$ compounds but did not provide detailed mode assignments. However, Sanivarapu *et al.*[20] explored the Raman spectroscopy of (REE = La, Pr, Nd)$(OH)_3$ and detected an OH stretching mode at ~3601 cm^{-1}. Given the analogy between $REE(OH)_3$ and our $YCl(OH)_2$, it is reasonable to assign the observed bands at 3516.8 and 3535.9 cm^{-1} to the OH stretching modes, corresponding to the two structurally nonequivalent hydrogen atoms in the structure (Figure 5a). At ambient pressure, the distances of the O1–H1 and the O2–H2 measure 0.78 and 0.65 Å, respectively. Since the shorter bond exhibits a higher vibration frequency, the bands observed at 3516.8 and 3535.9 cm^{-1} are designated as the ν_{OH1} and ν_{OH2} stretching modes, respectively.

The Raman spectra obtained at various pressures exhibit remarkable similarity. No signs of peak disappearance or the emergence of new peaks during the experimental process were observed, indicating the absence of phase transitions with changing pressure (Figures 7a and S1), aligned with the XRD results. Within the range of 100–1200 cm^{-1}, it was noted that, under certain pressure conditions, such as two Raman modes at ~730 and 830 cm^{-1} at ambient pressure (Figure S1), two Raman peaks merge, potentially leading to substantial uncertainty in peak fitting and, consequently, in the determination of their Raman shifts. However, apart from these instances, the Raman peaks below 1200 cm^{-1} consistently evolve with increasing pressure (Figure S1).

Notably, distinct behavior is observed for the two OH stretching modes, indicating a clear division in the pressure-Raman shift curve into two different regimes (Figure 7b). Between ambient pressure and 1.1 GPa, both ν_{OH1} and ν_{OH2} exhibit an increase with pressure at rates of 5.3 and 6.1 cm^{-1}/GPa, respectively. Beyond 1.1 GPa, both modes display a nonlinear increase with rising pressures up to 10.3 GPa. Fitting a quadratic function to the data resulted in $y = 3510.8\ (2) + 11.7\ (5)\ P - 0.48\ (4)\ P^2$ and $y = 3528.7\ (2) + 13.8\ (7)\ P - 0.57\ (6)\ P^2$ for ν_{OH1} and ν_{OH2}, respectively.

4. DISCUSSION

4.1. Compression Mechanism and Axial Negative Compressibility. The compressional behavior of $YCl(OH)_2$, observed through high-pressure SCXRD experiments, is shown in Figures 2 and 3. It is evident that the unit-cell parameters a, b, and c display distinct compressibility, with a being the most compressible and b being the least (Figure 3). This observation can be rationalized from the perspective of the crystal structure of $YCl(OH)_2$. As illustrated in Figure 5, the crystal structure primarily consists of YCl_2O_6 polyhedra. These polyhedra are interconnected to extend along the a–b plane, forming a sequence of polyhedral layers that are parallel to each other along the c direction (Figure 8a). However, Figure 3 demonstrates that the compressibility of the a-axis is significantly greater than that of the b-axis across the entire range of experimental pressures. This discrepancy arises because although the polyhedra are connected in both the a and b directions, the linkage occurs through face-sharing between polyhedra along the b direction, while edge-sharing occurs along the a direction (Figure 8a,b). As a result, the face-sharing linkage renders the b direction more rigid compared to the a direction. Furthermore, although the c-axis displays a higher compressibility than the b-axis, it is notably lower than the a-axis (Figure 3). In the c direction (Figure 8a), the bonding between the polyhedral layers is weak, leading to a reduction in layer spacing as the pressure increases up to 9.4 GPa. However, the primary effect of decreasing the layer spacing is a substantial increase in β rather than a reduction in the c-axis, resulting in less compression in the c direction compared to the a direction.

The most significant finding of this study is the negative linear compressibility in $YCl(OH)_2$. As depicted in Figure 2, the compression behavior of this crystal under hydrostatic

https://doi.org/10.1021/acs.inorgchem.3c03909
Inorg. Chem. 2024, 63, 2616–2626

Table 3. Atomic Distances, Coordination Polyhedron Volumes, and Interlayer Distances in $YCl(OH)_2$ up to 9.4 GPa[a]

P (GPa)	Y−O1a (Å)	Y−O1b (Å)	Y−O2a (Å)	Y−O2b (Å)	Y−Cl (Å)	Y−Cl (Å)*
0.0001	2.392 (1)	2.329 (1)	2.337 (1)	2.38 (1)	2.853 (1)	3.595 (1)
0.4 (1)	2.376 (16)	2.329 (18)	2.342 (11)	2.39 (4)	2.857 (5)	3.564 (7)
1.1 (1)	2.351 (16)	2.347 (18)	2.323 (12)	2.44 (4)	2.858 (5)	3.480 (7)
2.2 (1)	2.353 (16)	2.331 (17)	2.345 (12)	2.33 (4)	2.847 (5)	3.348 (7)
3.7 (1)	2.380 (30)	2.280 (30)	2.347 (16)	2.32 (5)	2.852 (8)	3.196 (11)
5.3 (1)	2.370 (30)	2.290 (30)	2.330 (16)	2.44 (6)	2.856 (9)	3.103 (11)
6.7 (1)	2.344 (19)	2.290 (20)	2.402 (17)	2.17 (5)	2.851 (6)	3.039 (7)
9.4 (1)	2.230 (60)	2.370 (80)	2.290 (40)	2.58 (18)	2.853 (17)	2.990 (20)

P (GPa)	Y−Y (Å)	average bond length (Å)	V (Å^3)	interlayer distance (Å)	distortion index
0.0001	3.6183 (1)	2.4846	25.9006	6.3343 (1)	0.07423
0.4 (1)	3.6166 (4)	2.4832	25.8273	6.3099 (2)	0.07526
1.1 (1)	3.6188 (3)	2.4814	25.5925	6.2626 (1)	0.07593
2.2 (1)	3.6266 (5)	2.4690	25.1688	6.1963 (2)	0.07663
3.7 (1)	3.6368 (3)	2.4696	25.0752	6.1200 (1)	0.07746
5.3 (1)	3.6401 (4)	2.4786	25.1895	6.0564 (2)	0.07603
6.7 (1)	3.6386 (4)	2.4563	24.4206	6.0088 (1)	0.08036
9.4 (1)	3.6302 (4)	2.4628	23.7681	5.9459 (2)	0.09156

[a]Numbers in parentheses represent standard deviations to the last significant digit.

pressure (using helium as the pressure-transmitting medium) exhibits an unconventional pattern. Initially, the unit-cell parameters *a*, *b*, and *c* decrease with increasing pressure up to 0.4 GPa. However, at higher pressures, *b* starts expanding, displaying negative compressibility, until 5.3 GPa. Subsequently, within the pressure range of 5.3−9.4 GPa, the compressional behavior of *b* becomes similar to that of *a* and *c*, and *b* gradually decreases with increasing pressure. In contrast to *b*, both *a* and *c* consistently decrease with increasing pressure throughout the entire experimental pressure range, while β gradually increases. The anomalous compressional behavior of *b* is reflected in the variation of the Y−Y atomic distances along the *b* direction. As illustrated in Figure 8d, from ambient pressure to 0.4 GPa, d_{Y-Y} distance gradually decreases with increasing pressure, followed by an increase from 0.4 to 5.3 GPa and subsequently a decrease with further increasing pressure (Figure 9), which aligns with the trajectory of *b* under high pressure (Figure 2b).

The anomalous compressibility of the *b*-axis can be attributed to two primary factors. First, as mentioned earlier, the unique arrangement of polyhedra within the $YCl(OH)_2$ crystal results in significantly lower compressibility for *b*-axis compared to *a* and *c*-axis. Second, at a critical pressure (0.4 GPa), the formation of O−H···O hydrogen bonds imparts sufficient rigidity to the *b* direction of the crystal, enabling it to have a mechanical response under pressure (0.4−5.3 GPa). As shown in Figure 8a, at ambient pressure, the two shortest H···O distances, H1···O2 and H2···O1, are 2.96 (4) and 2.79 (3) Å, respectively, slightly larger than the sum of the van der Waals radii of H and O atoms (2.72 Å).[25] This indicates that the oxygen-containing O−H1···O2 and oxygen-containing O−H2···O1 hydrogen bonds are either absent or weak at ambient pressure. However, as pressure increases to 0.4 GPa, the H···O distances likely decrease, leading to stronger hydrogen bonds. These hydrogen bonds interconnect, forming two zigzag hydrogen bond chains along the *b* direction (Figure 8a). The formation of this hydrogen bond chain causes the initially rigid *b* direction to exhibit negative compressibility within the pressure range of 0.4−5.3 GPa. It should be noted that the XRD data in this study do not provide sufficient information to determine the positions of hydrogen atoms in the structure under high pressure. Nevertheless, previous studies have revealed that high pressure induces a decrease in atomic distances, resulting in the formation of hydrogen bonds (*e.g.*, O−H···O and H···N) and the occurrence of negative linear compressibility in crystals.[26,27] Therefore, it is reasonable to speculate that the negative compressibility of *b* within the pressure range of 0.4−5.3 GPa in this study is caused by the formation of hydrogen bonds.

The Raman spectra obtained at high pressures further substantiate our hypothesis concerning hydrogen bond formation under such conditions. While Raman spectroscopy is not a direct method for assessing hydrogen bonding, the sensitivity of OH stretching (Raman active) wavenumbers to local molecular environments[28] makes it a valuable tool for probing hydrogen bonding interactions.[29] In Figure 7b and as previously noted, the pressure dependences of ν_{OH1} and ν_{OH2} exhibit a dichotomous nature with an inflection point occurring at 1.1 GPa.

Unfortunately, due to the challenge of precisely controlling pressure during helium loading into the sample chamber, we were unable to collect data between ambient pressure and 1.1 GPa. Nevertheless, the presence of an inflection at 1.1 GPa suggests that something other than increasing the pressure below 1.1 GPa is responsible for shifting the OH stretching mode. Certain studies have indicated that the formation of a hydrogen bond leads to a shift in the OH stretching mode.[30] Consequently, we attribute the spectroscopic manifestation between ambient pressure and 1.1 GPa to the formation of hydrogen bonds, specifically the interactions of the —H1···O2 and —H2···O1 mentioned earlier, which result in the negative compression of the *b*-axis of $YCl(OH)_2$ at 0.4−5.3 GPa. Beyond 1.1 and up to 10.3 GPa, the vibration frequencies of ν_{OH1} and ν_{OH2} consistently increase with the pressure, indicating that the hydrogen bonds formed at lower pressures remain intact.

It is noteworthy that the bulk modulus acquired for $YCl(OH)_2$ in this investigation (K_{T0} = 38.2 (18) GPa) closely resembles those found for certain layered metal iodates (such as $Fe(IO_3)_3$, K_{T0} = 36 (1) GPa).[31] Moreover, while linear negative compressibility has been observed in some metal iodates, it has been linked to the development of metavalent bonds, which differs from the negative compressibility of the *b*-axis noted for $YCl(OH)_2$ in this study.

Furthermore, as pressure surpasses 5.3 GPa, the compressional behavior of the *b*-axis returns to a normal state, indicating positive compression (Figure 2b). This suggests that the maximum pressure at which the —H2···O1 and —H1···O2

https://doi.org/10.1021/acs.inorgchem.3c03909
Inorg. Chem. 2024, 63, 2616−2626

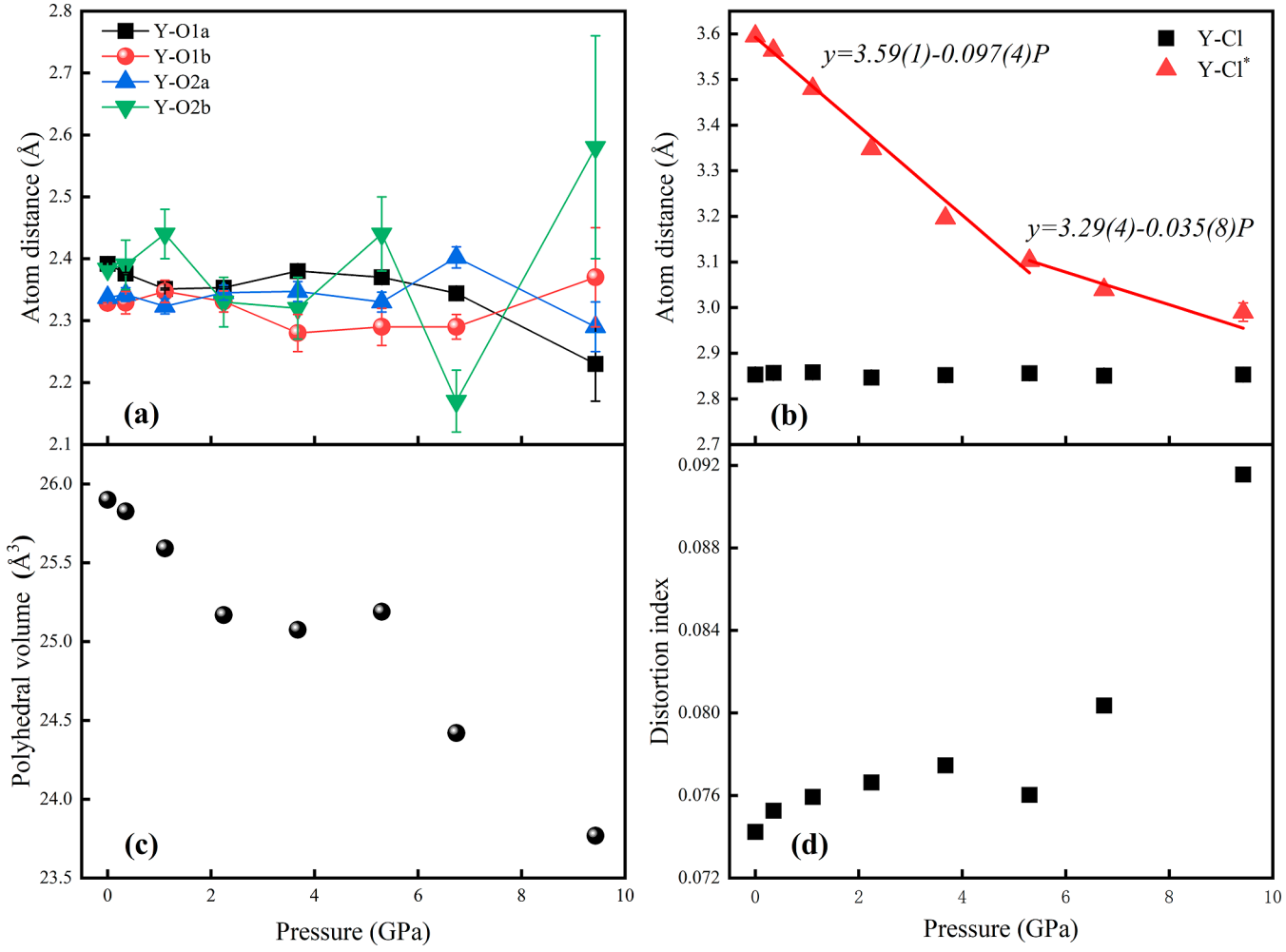

Figure 6. Bond lengths (a,b), polyhedral volume, and polyhedral distortion index of $YCl(OH)_2$ as a function of pressure. (a) Y−O1a (black squares), Y−O1b (red spheres), Y−O2a (blue triangles), and Y−O2b (green triangles). (b) Y−Cl (black squares) and Y−Cl* (red triangles). (c) Volume of the YCl_2O_6 polyhedron. (d) Distortion index of the YCl_2O_6 polyhedron. Error bars are smaller than the symbols when not shown.

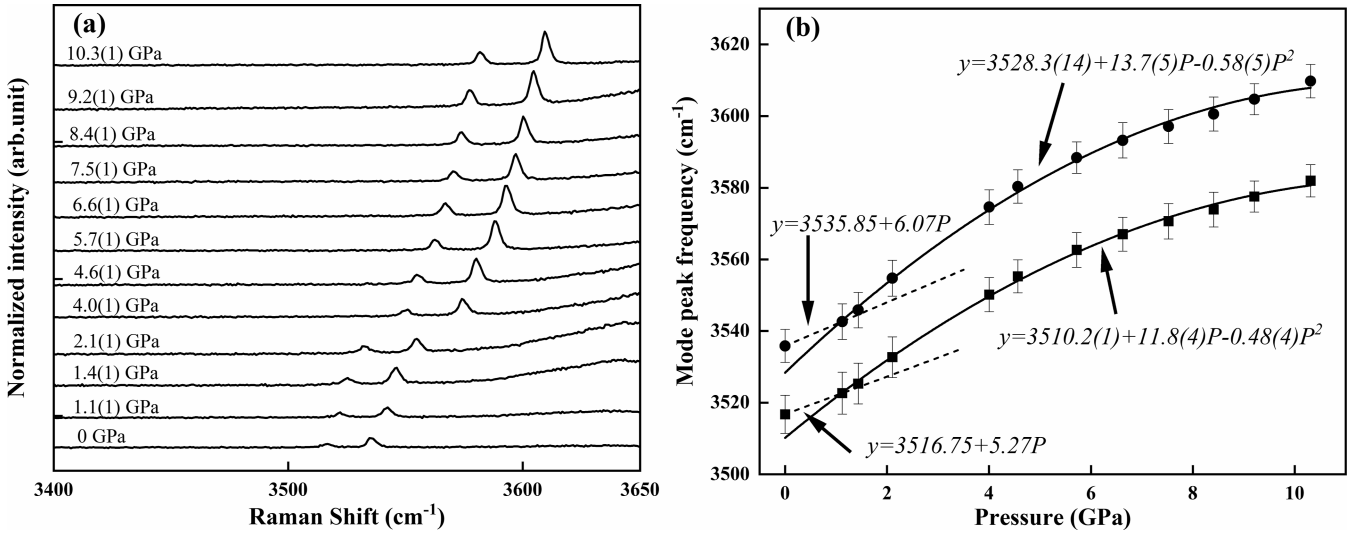

Figure 7. (a) Raman spectra of $YCl(OH)_2$ in the pressure range 0−10.3 GPa within the wavenumber range 3400−3650 cm^{-1}. (b) Mode peak frequencies of ν_{OH1} (square) and ν_{OH2} (ball) as a function of pressure. Dashed lines represent linear fitting to the data between ambient pressure and 1.1 GPa, while solid curves represent quadratic function fitting of the data within 1.1−10.3 GPa. The derived formula are shown nearby.

hydrogen bond chains can induce negative linear compressibility lies between 5.3 and 6.7 GPa (Figure 2b). Intriguingly, the pressure dependence of the YCl_2O_6 polyhedron volume and distortion index also exhibit an inflection at 5.3 GPa

https://doi.org/10.1021/acs.inorgchem.3c03909
Inorg. Chem. 2024, 63, 2616−2626

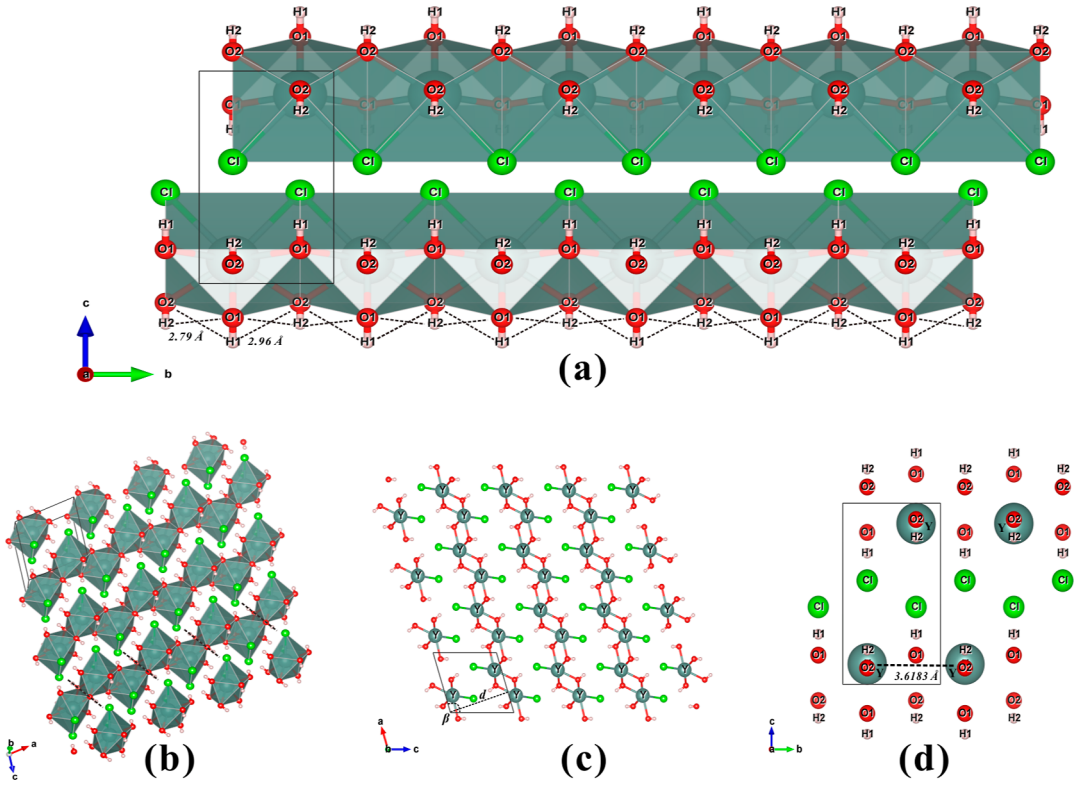

Figure 8. Crystal structure of $YCl(OH)_2$. (a) Projection along the *a*-axis to highlight the O−H···O hydrogen bond. (b) Dashed lines indicate edge-sharings between adjacent YO_6Cl_2 coordination polyhedra. (c) Projection along the *b*-axis shows the interlayer distances of the $YCl(OH)_2$ crystals, and the dashed lines are the interlayer distances of the $YCl(OH)_2$ crystals. (d) Projection along the *a*-axis to highlight the Y−Y atomic distance. Y atoms are dark green, Cl atoms are green, O atoms are red, and H atoms are pink, and the dashed line is the O−H···O hydrogen bond.

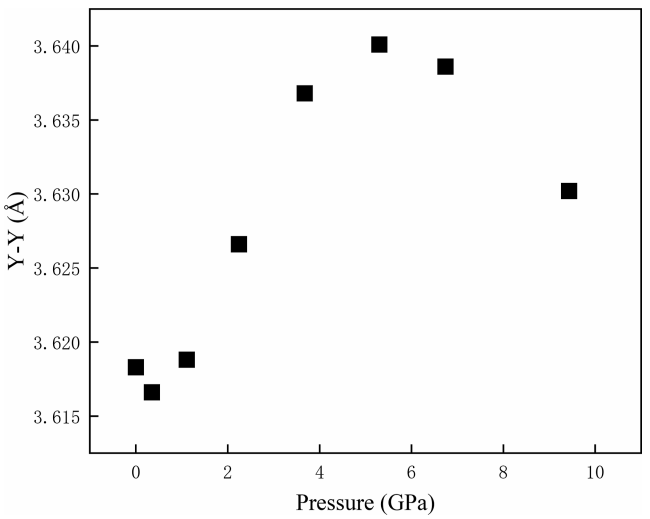

Figure 9. Y−Y atomic distances along the *b*-direction up to the 9.4 GPa range. Error bars are smaller than the symbols when not shown.

(Figure 6c,d). These anomalies could be attributed to a possible increase in the coordination number of Y^{3+}, caused by the decreasing Y−Cl* distance with increasing pressure. Figure 6b illustrates that from ambient pressure to 5.3 GPa, d_{Y-Cl*} decreases linearly with pressure at a rate of 0.097(4) Å/GPa. Subsequently, the decreasing rate diminishes to 0.035(8) Å/GPa after 5.3 GPa, and d_{Y-Cl*} (3.103 (11)−2.990 (20) Å) becomes comparable to that of d_{Y-Cl} (2.856 (9)−2.851 (6) Å). This suggests a strengthening interaction between Y and Cl* (potentially leading to bonding formation) when the pressure exceeds 5.3 GPa. Consequently, the newly formed strong interaction between Y and Cl* likely influences the compression and distortion of the initial YCl_2O_6 polyhedron (Figure 6c,d). Additionally, it could contribute to the closure of the interlayer gap (see the next section), and this structural adjustment ultimately results in positive compression along the *b*-axis.

Helium is commonly utilized as a pressure-transmitting medium, with numerous studies[32,33] demonstrating its ability to permeate specific crystalline compounds, thereby influencing their properties, such as compressional behavior. While the layered structure of $YCl(OH)_2$ seems capable of accommodating helium under high pressure, we dismiss helium penetration as the cause for the anomalous compression behavior of *b*-axis. Previous studies have suggested that helium penetration into the host structure could result in significant volume expansion as pressure increases.[32,33] However, our findings demonstrate a consistent decrease in the volume of $YCl(OH)_2$, without any sudden changes (Figure 3). Although the interlayer gap is anticipated as an ideal location for helium penetration, the steady reduction in interlayer spacing (as illustrated in Figure 10) at the very least implies that any helium penetration, if present, insignificantly affects the compression of the interlayer spacing, which is the most compressible section. Furthermore, the interlayer gap is not vacant—strong O−H1···Cl bonding links the polyhedral layers to form the structure, making it challenging to accommodate guest He atoms. Therefore, considering the volume compression data and the structural characteristics, helium is unlikely to penetrate the structure. Even if helium were to penetrate, it should not be considered

https://doi.org/10.1021/acs.inorgchem.3c03909
Inorg. Chem. 2024, 63, 2616−2626

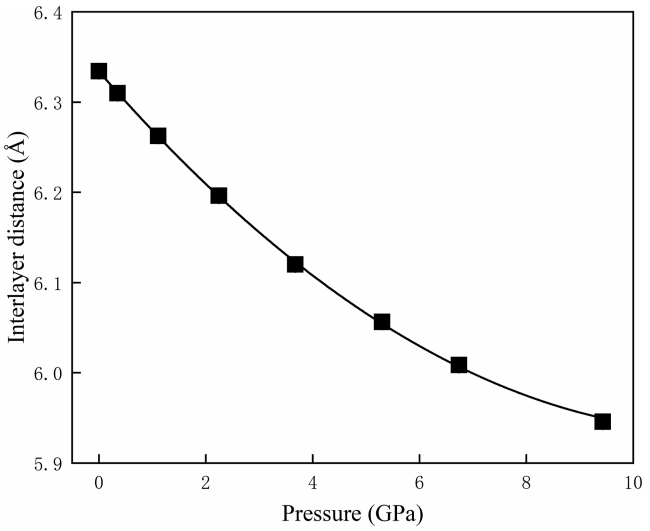

Figure 10. Interlayer spacing within the pressure range of 0−9.4 GPa. Error bars are smaller than the symbols when not shown.

the primary cause of the anomalous compressional behavior of *b*-axis.

4.2. Closure of the Interlayer Space. The size of the interlayer spacing plays a crucial role in determining the physical and chemical properties of layered materials, including stability and polarity.[34,35] Therefore, regulating the interlayer spacing of layer-structured materials is a hot topic in materials science.[36] In this study, we explored the interlayer spacing in $YCl(OH)_2$ under a high pressure. As shown in Figure 8c, we used $d = c \sin(180 - \beta)$ to indicate the variation of the interlayer spacing. At ambient pressure, d = 6.3343 (1) Å. As the pressure increased to the highest pressure of 9.4 GPa, d gradually decreased to 5.9459 (2) ppm (Figure 10). Thus, high pressure proves to be an effective method for regulating the interlayer spacing in this type of layered rare-earth hydroxyhalide. For $YCl(OH)_2$, fitting the data in Figure 10 with a quadratic function yielded d = 6.334 (1) − 0.0682 (1) P + 0.0029 (1) P^2 (R^2 = 0.9997). Moreover, the reduction in interlayer spacing renders a decrease in the distance between Y and the Cl* atoms. As shown in Figure 5, at ambient pressure, in the YCl_2O_6 polyhedron, the distance (d_{Y-Cl*}) between Y and its nearest Cl atom (Cl*) outside the polyhedron was 3.595 (1) Å, which is significantly larger than the distance between Y and Cl within the polyhedron (d_{Y-Cl} = 2.853 (1) Å). However, with increasing pressure, d_{Y-Cl*} gradually approached d_{Y-Cl} (Figure 6b). Within the pressure range of 5.3−9.4 GPa, d_{Y-Cl*} = 2.990 (20)−3.103 (11) Å, while d_{Y-Cl} = 2.851 (6)−2.903 (16) Å. Consequently, within this pressure range, the Cl^{*-} may bond to Y^{3+} in the YCl_2O_6 polyhedra, similar to the Cl^-, resulting in an increase in the coordination number of Y^{3+} from the initial 8 to 9. The increase in the coordination number of Y^{3+} leads to the closure of the interlayer spacing in $YCl(OH)_2$ (Figure 11).

5. CONCLUSIONS

This study employed a DAC combined with synchrotron SCXRD and Raman spectroscopy to investigate the compressional behavior of synthesized layered rare-earth hydroxyhalide ($YCl(OH)_2$) from atmospheric pressure to 9.4 GPa. The $P-V$ data were fitted to the BM3 EoS, yielding V_{T0} = 142.47 (1) Å^3, K_{T0} = 38.2 (18) GPa, and K'_{T0} = 9.8 (1). We observed a negative linear compressibility in $YCl(OH)_2$ along the *b*-axis, and this anomalous compression behavior of *b* is attributed to two factors. First, the arrangement of the YCl_2O_6 polyhedra inside the $YCl(OH)_2$ crystal determines that the compression of *b* is significantly lower than that of *a* and *c*. Second, at a critical pressure (0.4 GPa), the formation of O−H···O hydrogen bonds imparts sufficient rigidity to the *b* direction of the crystal, resulting in mechanical response upon compression (0.4−5.3 GPa). Additionally, we discussed the reduction of interlayer spacing (d) in $YCl(OH)_2$ under high pressure and derived a formula to describe the spacing as a function of pressure: d = 6.334 (1) − 0.0682 (1) P + 0.0029 (1) P^2, R^2 = 0.9997. Finally, the increase in the coordination number of Y^{3+} from 8 to 9 resulted from the reduction of interlayer spacing, leading to interlayer gap closure at pressures higher than 5.3 GPa.

■ ASSOCIATED CONTENT

Supporting Information

The Supporting Information is available free of charge at https://pubs.acs.org/doi/10.1021/acs.inorgchem.3c03909.

Raman spectroscopy of $YCl(OH)_2$ in the pressure range of 0−10.3 GPa within the wavenumber range of 100−1200 cm^{-1} and pressure-dependent Raman shift for $YCl(OH)_2$ under hydrostatic condition within the wavenumber range of 100−1200 cm^{-1}. CIF files for each pressure point (PDF)

Accession Codes

CCDC 2322542−2322549 contains the supplementary crystallographic data for this paper. These data can be

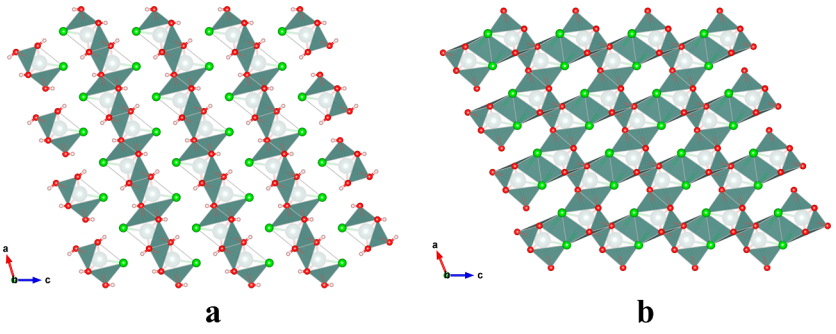

Figure 11. (a) Polyhedral layers parallel to the *c*-axis in the crystal structure of $YCl(OH)_2$ at ambient pressure; (b) crystal structure of $YCl(OH)_2$ at 9.4 GPa, where an increase in the coordination number of Y^{3+} leads to the closure of interlayer spaces. Y atoms are represented in dark green, Cl atoms in green, and O atoms in red.

https://doi.org/10.1021/acs.inorgchem.3c03909
Inorg. Chem. 2024, 63, 2616−2626

obtained free of charge via www.ccdc.cam.ac.uk/data_request/cif, or by emailing data_request@ccdc.cam.ac.uk, or by contacting The Cambridge Crystallographic Data Centre, 12 Union Road, Cambridge CB2 1EZ, UK; fax: +44 1223 336033.

AUTHOR INFORMATION

Corresponding Authors

Jingui Xu − *Key Laboratory of High-Temperature and High-Pressure Study of the Earth's Interior, Institute of Geochemistry, Chinese Academy of Sciences, Guiyang 550081 Guizhou, China*; Email: xujingui@mail.gyig.ac.cn

Dawei Fan − *Key Laboratory of High-Temperature and High-Pressure Study of the Earth's Interior, Institute of Geochemistry, Chinese Academy of Sciences, Guiyang 550081 Guizhou, China*; Email: fandawei@mail.gyig.ac.cn

Authors

Mengzeng Wu − *Key Laboratory of High-Temperature and High-Pressure Study of the Earth's Interior, Institute of Geochemistry, Chinese Academy of Sciences, Guiyang 550081 Guizhou, China; University of Chinese Academy of Sciences, Beijing 100049, China*; orcid.org/0009-0006-9577-1490

Dongzhou Zhang − *Center for Advanced Radiation Sources, University of Chicago, Chicago, Illinois 60437, United States*

Yi Zhou − *School of Geoscience and Technology, Southwest Petroleum University, Chengdu 610500 Sichuan, China*

Wei Chen − *Key Laboratory of High-Temperature and High-Pressure Study of the Earth's Interior, Institute of Geochemistry, Chinese Academy of Sciences, Guiyang 550081 Guizhou, China; University of Chinese Academy of Sciences, Beijing 100049, China*

Shanrong Zhang − *Key Laboratory of High-Temperature and High-Pressure Study of the Earth's Interior, Institute of Geochemistry, Chinese Academy of Sciences, Guiyang 550081 Guizhou, China; University of Chinese Academy of Sciences, Beijing 100049, China*

Qifa Zhong − *Key Laboratory of High-Temperature and High-Pressure Study of the Earth's Interior, Institute of Geochemistry, Chinese Academy of Sciences, Guiyang 550081 Guizhou, China; University of Chinese Academy of Sciences, Beijing 100049, China*

Complete contact information is available at: https://pubs.acs.org/10.1021/acs.inorgchem.3c03909

Notes

The authors declare no competing financial interest.

ACKNOWLEDGMENTS

Sincere thanks go to S.N. Tkachev and Bin Yang for their help with gas loading and high-pressure Raman spectroscopy experiments. This project was supported by the Hundred Talents Program of the Chinese Academy of Sciences, the National Natural Science Foundation of China (grant no. 42172048), the Guizhou Provincial Science and Technology Projects (QKHPTRC-YQK[2023]035 and QKHJC-ZK[2021] ZD042), and Guizhou Provincial 2020 and 2021 Science and Technology Subsidies (nos. GZ2020SIG and GZ2021SIG). Y.Z. acknowledges support from the National Natural Science Foundation of China (grant no. 42302114) and the Sichuan Provincial Natural Science Foundation Project (no. 2022NSFSC0256). Portions of this work were supported by COMPRES under NSF Cooperative Agreement EAR-1661511 and by GSECARS through NSF grant EAR-1634415. This research used resources of the Advanced Photon Source, a U.S. Department of Energy (DOE) Office of Science User Facility operated for the DOE Office of Science by Argonne National Laboratory under contract no. DE-AC02-06CH11357.

REFERENCES

(1) Dushyantha, N.; Batapola, N.; Ilankoon, I. M. S. K.; Rohitha, S.; Premasiri, R.; Abeysinghe, B.; Ratnayake, N.; Dissanayake, K. The story of rare earth elements (REEs): Occurrences, global distribution, genesis, geology, mineralogy and global production. *Ore Geol. Rev.* **2020**, *122*, 103521.

(2) Balaram, V. Rare earth elements: A review of applications, occurrence, exploration, analysis, recycling, and environmental impact. *Geosci. Front.* **2019**, *10*, 1285−1303.

(3) Gulley, A. L.; Nassar, N. T.; Xun, S. China, the United States, and competition for resources that enable emerging technologies. *Proc. Natl. Acad. Sci. U.S.A.* **2018**, *115*, 4111−4115.

(4) Song, X.; Zhang, J.; Yue, M.; Li, E.; Zeng, H.; Lu, N.; Zhou, M.; Zuo, T. Technique for preparing ultrafine nanocrystalline bulk material of pure rare-earth metals. *Adv. Mater.* **2006**, *18*, 1210−1215.

(5) Liang, J.; Ma, R.; Sasaki, T. Layered rare earth hydroxides (LREHs): synthesis and structure characterization towards multi-functionality. *Dalton Trans.* **2014**, *43*, 10355−10364.

(6) Geng, F.; Xin, H.; Matsushita, Y.; Ma, R.; Tanaka, M.; Izumi, F.; Iyi, N.; Sasaki, T. New Layered Rare-Earth Hydroxides with Anion-Exchange Properties. *Chemistry* **2008**, *14*, 9255−9260.

(7) Lee, K.-H.; Byeon, S.-H. Extended Members of the Layered Rare-Earth Hydroxide Family, $RE_2(OH)_5NO_3{\cdot}nH_2O$ (RE = Sm, Eu, and Gd): Synthesis and Anion-Exchange Behavior. *Eur. J. Inorg. Chem.* **2009**, *2009*, 929−936.

(8) Lee, K.-H.; Byeon, S.-H. Synthesis and Aqueous Colloidal Solutions of $RE_2(OH)_5NO_3{\cdot}nH_2O$ (RE = Nd and La). *Eur. J. Inorg. Chem.* **2009**, *2009*, 4727−4732.

(9) McIntyre, L. J.; Jackson, L. K.; Fogg, A. M. $Ln_2(OH)_5NO_3{\cdot}xH_2O$ (Ln = Y, Gd−Lu): A Novel Family of Anion Exchange Intercalation Hosts. *Chem. Mater.* **2008**, *20*, 335−340.

(10) Li, F.; Duan, X. *Layered Double Hydroxides. Applications of Layered Double Hydroxides*; Springer Berlin Heidelberg, 2006; pp 193−223.

(11) Zhang, Q.; Chen, C.; Li, N. N.; Huang, Q.; He, Y.; Liu, X. Q.; Wang, B. H.; Zhang, D. Z.; Kim, D. Y.; Wang, Y. G.; Xu, B.; Yang, W. G. Pressure Impact on the Crystal Structure, Optical, and Transport Properties in Layered Oxychalcogenides BiCuChO (Ch = S, Se). *J. Phys. Chem. C* **2018**, *122*, 15929−15936.

(12) Wang, X.; Liu, X. High pressure: a feasible tool for the synthesis of unprecedented inorganic compounds. *Inorg. Chem. Front.* **2020**, *7*, 2890−2908.

(13) Pei, S.; Wang, Z.; Xia, J. High pressure studies of 2D materials and heterostructures: A review. *Mater. Des.* **2022**, *213*, 110363.

(14) Klevtsova, R. F.; Klevtsov, P. V. X-ray diffraction study of a new modification of yttrium hydroxychloride $Y(OH)_2Cl$. *J. Struct. Chem.* **1967**, *7*, 524−527.

(15) Shen, G.; Smith, J. S.; Kenney-Benson, C.; Klotz, S. Calibration of ruby (Cr^{3+}:Al_2O_3) and Sm^{2+}:SrFCl luminescence lines from the melting of mercury: constraints on the initial slopes. *High Press Res.* **2021**, *41*, 175−183.

(16) Zhang, D. Z.; Dera, P. K.; Eng, P. J.; Stubbs, J. E.; Zhang, J. S.; Prakapenka, V. B.; Rivers, M. L. High Pressure Single Crystal Diffraction at P$\hat{X}$2. *J. Vis. Exp.* **2017**, *119*, 54660.

(17) Sheldrick, G. M. A short history of SHELX. *Acta Crystallogr. A* **2008**, *64*, 112−122.

(18) Dolomanov, O. V.; Bourhis, L. J.; Gildea, R. J.; Howard, J. A. K.; Puschmann, H. OLEX2: a complete structure solution, refinement and analysis program. *J. Appl. Crystallogr.* **2009**, *42*, 339−341.

(19) Momma, K.; Izumi, F. VESTA 3 for three-dimensional visualization of crystal, volumetric and morphology data. *J. Appl. Crystallogr.* **2011**, *44*, 1272−1276.

(20) Sanivarapu, S. R.; Lawrence, J. B.; Sreedhar, G. Role of Surface Oxygen Vacancies and Lanthanide Contraction Phenomenon of $Ln(OH)_3$ (Ln = La, Pr, and Nd) in Sulfide-Mediated Photoelectrochemical Water Splitting. *ACS Omega* **2018**, *3* (6), 6267−6278.
(21) Angel, R. J.; Alvaro, M.; Gonzalez-Platas, J. EosFit7c and a Fortran module (library) for equation of state calculations. *Z. Kristallogr Cryst. Mater.* **2014**, *229*, 405−419.
(22) Angel, R. J. Equations of state. *High Press Res.* **2000**, *41*, 35−59.
(23) Kroumova, E.; Aroyo, M. I.; Perez-Mato, J. M.; Kirov, A.; Capillas, C.; Ivantchev, S.; Wondratschek, H. Bilbao crystallographic server: Useful databases and tools for phase-transition studies. *Phase Transit.* **2003**, *76* (1−2), 155−170.
(24) Zehnder, R. A.; Clark, D. L.; Scott, B. L.; Donohoe, R. J.; Palmer, P. D.; Runde, W. H.; Hobart, D. E. Investigation of the Structural Properties of an Extended Series of Lanthanide Bishydroxychlorides $Ln(OH)_2Cl$ (Ln = Nd-Lu, except Pm and Sm). *Inorg. Chem.* **2010**, *49* (11), 4781−4790.
(25) Bondi, A. van der Waals Volumes and Radii. *J. Phys. Chem. C* **1964**, *68*, 441−451.
(26) Szafranski, M. Large Negative Linear Compressibility Triggered by Hydrogen Bonding. *J. Phys. Chem. C* **2020**, *124*, 11631−11638.
(27) Qiao, Y.; Wang, K.; Yuan, H.; Yang, K.; Zou, B. Negative Linear Compressibility in Organic Mineral Ammonium Oxalate Monohydrate with Hydrogen Bonding Wine-Rack Motifs. *J. Phys. Chem. Lett.* **2015**, *6*, 2755−2760.
(28) Auer, B.; Kumar, R.; Schmidt, J. R.; Skinner, J. L. Hydrogen bonding and Raman, IR, and 2D-IR spectroscopy of dilute HOD in liquid D_2O. *Proc. Natl. Acad. Sci. U.S.A.* **2007**, *104* (36), 14215−14220.
(29) Liu, S. L.; Zhang, M. Z.; Huang, B. K.; Wu, N. N.; Ouyang, S. L. Raman Spectroscopy for the Competition of Hydrogen Bonds in Ternary (H_2O-THF-DMSO) Aqueous Solutions. *Molecules* **2019**, *24* (20), 3666.
(30) Kolesov, B. A. Hydrogen Bonds: Raman Spectroscopic Study. *Int. J. Mol. Sci.* **2021**, *22* (10), 5380.
(31) Liang, A.; Turnbull, R.; Errandonea, D. A review on the advancements in the characterization of the high-pressure properties of iodates. *Prog. Mater. Sci.* **2023**, *136*, 101092.
(32) Yagi, T.; Iida, E.; Hirai, H.; Miyajima, N.; Kikegawa, T.; Bunno, M. High-pressure behavior of a SiO_2 clathrate observed by using various pressure media. *Phys. Rev. B* **2007**, *75* (17), 174115.
(33) Lloyd, A. J., II; Hester, B. R.; Baxter, S. J.; Ma, S.; Prakapenka, V. B.; Tkachev, S. N.; Park, C.; Wilkinson, A. P. Hybrid Double Perovskite Containing Helium: $[He_2]$ $[CaZr]F_6$. *Chem. Mater.* **2021**, *33* (9), 3132−3138.
(34) Sakuma, H.; Suehara, S. Interlayer bonding energy of layered minerals: Implication for the relationship with friction coefficient. *J. Geophys. Res. Solid Earth.* **2015**, *120*, 2212−2219.
(35) Giese, R. F. The Electrostatic Interlayer Forces of Layer Structure Minerals. *Clays Clay Miner.* **1978**, *26*, 51−57.
(36) Ding, Y.; Zeng, M.; Zheng, Q.; Zhang, J.; Xu, D.; Chen, W.; Wang, C.; Chen, S.; Xie, Y.; Ding, Y.; Zheng, S.; Zhao, J.; Gao, P.; Fu, L. Bidirectional and reversible tuning of the interlayer spacing of two-dimensional materials. *Nat. Commun.* **2021**, *12*, 5886.

https://doi.org/10.1021/acs.inorgchem.3c03909
Inorg. Chem. 2024, 63, 2616−2626